MRI-Guided Diffuse Optical Spectroscopy of Malignant and Benign Breast Lesions[1]

Vasilis Ntziachristos[*,†], *A. G. Yodh*[‡], *Mitchell D. Schnall*[§] *and Britton Chance*[†]

Departments of *Bioengineering, †Biochemistry/Biophysics, ‡Physics and Astronomy, §Radiology, University of Pennsylvania, Philadelphia, PA 19104-6059, USA

Abstract

We present the clinical implementation of a novel hybrid system that combines magnetic resonance imaging (MRI) and near-infrared (NIR) optical measurements for the noninvasive study of breast cancer *in vivo*. Fourteen patients were studied with a MR-NIR prototype imager and spectrometer. A diffuse optical tomographic scheme employed the MR images as *a priori* information to implement an image-guided NIR localized spectroscopic scheme. All patients who entered the study also underwent gadolinium-enhanced MRI and biopsy so that the optical findings were cross-validated with MR readings and histopathology. The technique quantified the oxy- and deoxyhemoglobin of five malignant and nine benign breast lesions *in vivo*. Breast cancers were found with decreased oxygen saturation and higher blood concentration than most benign lesions. The average hemoglobin concentration ([H]) of cancers was 0.130±0.100 mM, and the average hemoglobin saturation (Y) was 60±9% compared to [H]=0.018±0.005 mM and Y=69±6% of background tissue. Fibroadenomas exhibited high hemoglobin concentration [H]=0.060±0.010 mM and mild decrease in oxygen saturation Y=67±2%. Cysts and other normal lesions were easily differentiated based on intrinsic contrast information. This novel optical technology can be a significant add-on in MR examinations and can be used to characterize functional parameters of cancers with diagnostic and treatment prognosis potential. It is foreseen that the technique can play a major role in functional activation studies of brain and muscle as well.

Introduction

Light offers unique wavelength-dependent contrast mechanisms in tissues; the scattering, absorption, and fluorescence of intrinsic tissue chromophores or extrinsically administered chromophores contain information about anatomy, physiology, biochemistry, and molecular function [1]. These unique contrast mechanisms have driven recent developments for imaging deep into tissue using near-infrared (NIR) radiation [2-4]. NIR light can penetrate several centimeters into tissue before it is attenuated below detection. The main intrinsic mechanisms of NIR light attenuation in tissue are the scattering due to index of refraction variations of the cellular organelles [5,6], and absorption mainly due to oxy- and deoxyhemoglobin, and in lesser degree due to water and lipids [5].

Diffusion theory [7] has been employed over the last decade to model the propagation of highly scattered NIR photons in deep tissue and provided rigorous mathematical models for noninvasive quantification of the optical properties of large organs. Quantification of the average optical properties of tissue at multiple wavelengths constitutes diffuse optical spectroscopy (DOS), which has been used to investigate muscle [8,9], brain activation [10-12], and assess physiological responses from normal and malignant breast tissues [5]. The combination of multiple NIR light measurements through tissue at several projections, using appropriate mathematical models based on diffusion theory, led to a new tomographic technique termed diffuse optical tomography (DOT). This technique has been recently applied clinically to produce quantified tomographic images of tissue chromophore concentrations in imaging brain function [4] and breast cancer [2,3].

In this paper, we present the clinical application of a method that combines concurrent optical and magnetic resonance (MR) measurements to perform magnetic resonance imaging (MRI)-guided DOS and noninvasively retrieve functional tumor characteristics in deep tissue. This approach originates a novel imaging and spectroscopic modality that merges the information content of MR and optical contrast into one scanner. Concurrent DOT and MRI as stand-alone imaging modalities have been performed recently for validation of DOT performance [3].

But the combination of the optical and MR measurements into *the same* tomographic scheme yields additional benefits that cannot be achieved simply by acquiring MR and optical images as *stand-alone* techniques. This is because the use of *a priori* information, such as the anatomical or functional information from MRI, can significantly improve the quantification accuracy of the optical method by constraining the DOT inverse problem [13-15]. Therefore, tissue chromophores and fluorochromes associated with function and disease can be quantified with high accuracy and resolution compared to other noninvasive techniques. The optical and MR examinations are fully compatible and, given the cost efficiency of optical systems, it would be anticipated that hybrid MR–optical systems could be easily implemented to augment the information content of the MR examination.

This work had three aims. The first aim was to demonstrate the first reported clinical implementation of MR-guided DOS, and illustrate practical aspects of the technique. The second aim was to noninvasively quantify the optical properties of breast tumors *in vivo* and obtain localized measurements of hemoglobin concentration and oxygenation. Finally, the third aim was to obtain insight on the distribution of cancer-associated optically detected intrinsic signals. The assessment of tumor function, i.e., vascularization and oxygenation status, can be associated with angiogenesis and cancer-specific hypoxia and may correlate with malignancy and metastatic potential. Localized DOS may be the method of choice for such investigations because it can offer higher quantification accuracy than the existing conventional NIR spectroscopic and tomographic methods.

The remainder of this paper briefly describes the hybrid MR–DOT instrument and breast examination protocol, presents the theory and practical aspects of localized DOS, and reports our findings on 14 patients.

Materials and Methods

MR–DOT Instrument

The MR scanner employed was a 1.5-T imager (Signa; GE Medical Systems, Milwaukee, WI), version 5.4 software. The optical instrument was a custom-built time domain optical imager and spectrometer that has been described in the past [12,16]. In brief, the optical instrument used laser diodes to produce short photon pulses (50 ps full width at half maximum) that excite the tissue under investigation. Two wavelengths at 780 and 830 nm were used. At more recent examinations, an additional wavelength (690 nm) was added. The average power for all wavelengths was ~40 μW (Food and Drug Administration Class I). The pulse repetition rate was 5 MHz. An optical switch (Dicon Fiberoptics, Richmond, CA) was used to time-multiplex the source light to 24 positions on the breast using single 100/140 μm core/

clad graded index fibers. The detection optical system used eight fiber bundles for parallel photon collection. Photon detection was achieved using the R5600U-50 GaAs photomultiplier tubes (Hamamatsu, Bridgewater, NJ). The arrival of single photons was time-resolved using the SPC-300 single-photon counting time-correlating system (PicoQuant, Berlin, Germany). Both source fibers and fiber bundles were 10 m long so that the instrument was placed outside the MR scanner room to avoid electromagnetic interference.

During examination, the breast was compressed gently between two plates, as shown in Figure 1. The plates held the optical fibers and the receiving MR radio-frequency coils [17]. Specially designed fiducials containing water and $CuSO_4$ were attached onto the plates. The fiducials appear on the MR images for registration purposes. All source fibers were mounted on one plate, forming a 3×8 grid array with adjacent fiber separations of 1.25 cm. All detector fiber bundles were mounted on the other plate, forming a 2×4 grid array with adjacent fiber separation of 2.5 cm.

Localized DOS

The optical instrument employed in this study can perform DOT, DOS, and image-guided DOS. Localized DOS can be implemented by combining a typical DOT problem at multiple wavelengths with *a priori* information (provided herein by MRI) and effectively converts an "imaging" problem to a lesion "characterization" problem. In the following, we briefly explain the basic formulation steps of localized DOS, for presentation completeness.

DOT We begin this description from the simple perturbative tomographic problem, which can be written in matrix form as:

$$
\begin{bmatrix}
\phi_{sc}(\vec{r}_{s1}, \vec{r}_{d1}, \omega_1) \\
\vdots \\
\phi_{sc}(\vec{r}_{sm}, \vec{r}_{dm}, \omega_m)
\end{bmatrix}
=
\begin{bmatrix}
W_{11} & \cdots & W_{1n}^a \\
\vdots & \ddots & \vdots \\
W_{m1} & \cdots & W_{mn}
\end{bmatrix}
\cdot
\begin{bmatrix}
\delta\mu_a(\vec{r}_1) \\
\vdots \\
\delta\mu_a(\vec{r}_n)
\end{bmatrix}.
$$

(1)

The left-most vector of Eq. (1) is the measurement vector, i.e., it contains measurements of the light detected at the tissue boundary at position $\vec{r}_d$, due to a source at position $\vec{r}_s$. In the general case, the source light can be modulated at different frequencies ω; therefore, the measurement vector contains measurements of multiple source detector pairs at different modulation frequencies. For o number of sources, p number of detectors, and q number of frequencies, the length of the measurement vector is m=o×p×q.

The right-most vector is the vector of unknowns. For tomographic purposes, the volume of interest is segmented into a number of voxels. The volume has an average absorption coefficient μ_{a0} and an average diffusion coefficient D_0. Each voxel is then associated with an unknown absorption perturbation relative to μ_{a0}. Solving the problem
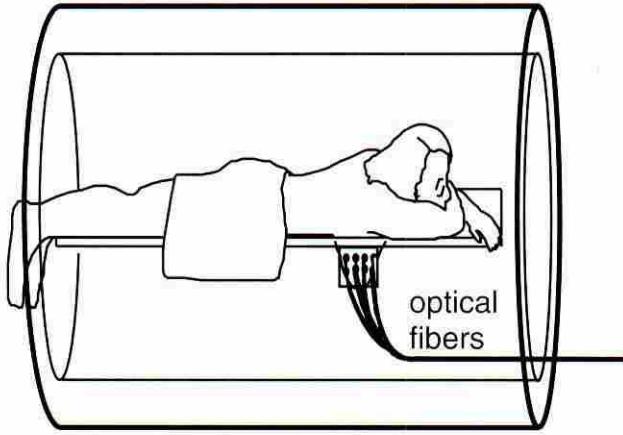
Figure 1. *Patient placement into the MR bore. Source fibers were attached on the inner side of the pedant breast, and detector fiber bundles were placed on the outer side of the breast, using appropriate plates that compress the breast softly. Light was shined sequentially through the 24 source fibers and acquired in parallel on the other side by the detector fiber bundles so that multiple projections were collected for each source fiber.*

for the unknown optical properties retrieves a three-dimensional quantified image of the absorption distribution. For n_x, n_y, n_z voxels along the three dimensions, the vector of unknowns is $n=n_x \times n_y \times n_z$. For three-dimensional reconstructions, this vector can easily become very large. Eq. (2) assumes that no diffusion coefficient perturbations exist for simplicity. Diffusion perturbations can be handled similarly to absorption perturbations and their contribution can be approximated [18] as a linear superposition to Eq. (1).

The matrix in the middle is the weight matrix, which maps the space of unknowns to the space of measurements. Each of the elements W_{mn} describes the effect that the optical property perturbation of voxel n has on the measurement m. The exact form of the weights is given elsewhere [18].

Using a priori information Eq. (1) represents the general formulation of DOT using perturbation theory. Let us assume that we superimpose a stack of MR images onto the DOT discretization mesh $n_x \times n_y \times n_z$. Then we can relate each optical mesh voxel with different breast tissues. For example, a group of voxels could coincide with purely adipose tissue, others with purely parenchymal tissue, and others with mixed patches of adipose and parenchymal tissues as shown in Figure 2. Figure 2 depicts a two-dimensional representation of the three-dimensional problem and uses large DOT voxels for presentation reasons. Then we can assume that all optical mesh voxels related with the same tissue type have the same absorption perturbation $\delta\mu_a(\vec{r})$. In practical terms, this assumption allocates a different average $\delta\mu_a(\vec{r})$ to each of the selected tissue types. Hence, the number of unknowns in Eq. (1) reduces to the number T of unknown tissue types assumed (e.g., adipose, parenchymal, tumor, mixed, and so forth). Accordingly, all the columns of the weight matrix in Eq. (1)

that correspond to voxels of the same tissue structure can be grouped together and Eq. (1) can be written as:

$$
\begin{bmatrix} \phi_{sc}(\vec{r}_{s1},\vec{r}_{d1},\omega_1) \\ \vdots \\ \phi_{sc}(\vec{r}_{sm},\vec{r}_{dm},\omega_m) \end{bmatrix}
$$

$$
= \begin{bmatrix} \sum_{t1=1}^{Q1} W_{1,t1}^a & \sum_{t2=1}^{Q2} W_{1,t2}^a & \cdots & \sum_{tT=1}^{QT} W_{1,tT}^a \\ \vdots & \vdots & & \vdots \\ \sum_{t1=1}^{Q1} W_{m,t1}^a & \sum_{t2=1}^{Q2} W_{m,t2}^a & \cdots & \sum_{tT=1}^{QT} W_{m,tT}^a \end{bmatrix} \cdot \begin{bmatrix} \delta\mu_a^{Tissue1} \\ \delta\mu_a^{Tissue2} \\ \vdots \\ \delta\mu_a^{TissueT} \end{bmatrix}, \quad (2)
$$

where $Q1$, $Q2$, ... QT indicate the number of voxels corresponding to each of the T different tissues assumed. Eq. (2) typically reduces the number of unknowns by three orders of magnitude while it employs the same number of measurements used in the DOT problem. Therefore, it produces a highly overdetermined system of equations (i.e., a system of equations with significantly more measurements than unknowns) and considerably reduces the complexity and computation requirements of the inversion compared to the corresponding DOT problem. Eq. (2) can be solved with higher accuracy than the typical DOT inversion problems [13,14], which are usually underdetermined (i.e., have more unknowns than measurements) and therefore cannot be
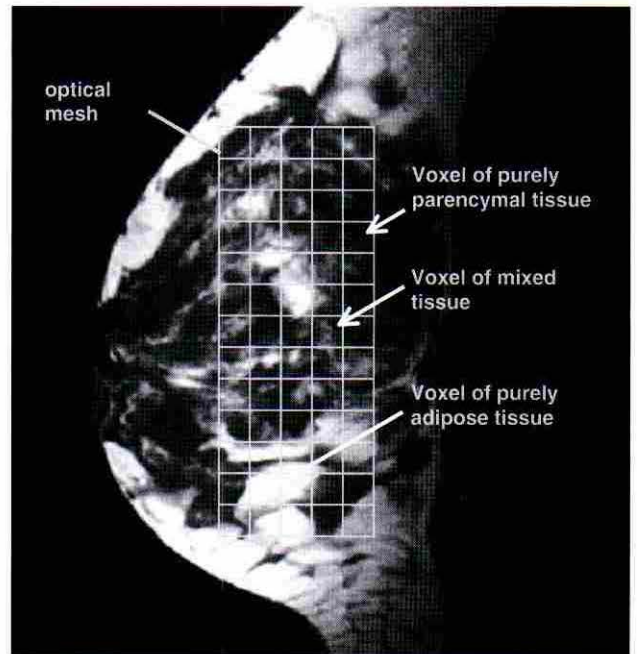

Figure 2. *Two-dimensional representation of the three-dimensional problem of overlaying the optical mesh onto the MR image. Different voxels of the optical mesh correspond to different tissue types or combinations of them. By setting appropriate thresholds, each of the optical mesh voxels can be assigned to one tissue type that has an average absorption coefficient and an average reduced scattering coefficient that is common to all voxels of the same tissue type.*

inverted with high fidelity, especially in the case of hetero-geneous, tissue-like media [19].

Two-Tissue Merit Function

Eq. (2) serves as an example of a localized DOS application. In practice, different segmentation schemes will yield different sets of unknowns. The different possibilities further expand if diffusion perturbations are implemented as well. In this work, we opted for a merit function that would be physiologically relevant while preserving maximum inversion robustness. We found a two-tissue merit function, which fits only for the absorption perturbation of two tissues (struc-tures), to be a balanced choice of available alternatives. We assumed that the breast consisted of a "background structure" which was a mix of adipose, parenchymal, and other tissues and the "tumor structure" which incorporated voxels that corresponded only to tumors. In accordance to Eq. (2), the selected merit function can be written as:

$$
\begin{bmatrix} \phi_{sc}(\vec{r}_{s1}, \vec{r}_{d1}, \omega_1) \\ \vdots \\ \phi_{sc}(\vec{r}_{sm}, \vec{r}_{dm}, \omega_m) \end{bmatrix} = \begin{bmatrix} \sum_{t1=1}^{Q1} W_{1,t1}^a & \sum_{t2=1}^{Q2} W_{1,t2}^a \\ \vdots & \vdots \\ \sum_{t1=1}^{Q1} W_{m,t1}^a & \sum_{t2=1}^{Q2} W_{m,t2}^a \end{bmatrix} \cdot \begin{bmatrix} \delta\mu_a^{Tumor} \\ \delta\mu_a^{Backgr} \end{bmatrix},
$$

(3)

where $Q1$ are the optical mesh voxels coinciding with the tumor structure and $Q2$ all the remaining voxels. The two-tissue merit function has been experimentally evaluated in the past using single absorbers embedded in otherwise homogeneous phantoms, which simulated the geometry and average optical properties of the breast [15,20], and demonstrated linear response and good quantification accuracy to absorption values up to 0.15 cm^{-1}. This merit function has been also evaluated using simulated data on highly heterogeneous backgrounds [21] and demonstrated quantification accuracy within $\pm5\%$ of the actual absorption of the tumor structure, for varying background heterogeneity, i.e., the ratio and the spatial appearance of adipose and parenchymal tissue.

Eq. (3) does not score independently the composition of different tissues involved in the background structure but assumes an average contribution of all background tissues. The main postulation is that the absorption coefficient of the background optical heterogeneity attains a distribution, which, although is not necessarily random, perturbs the propagating photon wavefront randomly so that this pertur-bation appears at the detection front as spatially uncorre-lated noise. Furthermore, Eq. (3) assumes a similar random pattern for the diffusion coefficient heterogeneity $\delta D(\vec{r})$. Some tumors will actually exhibit scattering changes due to neoplastic structural malformations [6]. The underlying assumption of Eq. (3) is that the $\delta D(\vec{r})$ of tumors contributes to a general random pattern of $\delta D(\vec{r})$ variation seen along the breast tissue due to the ductal system or the changes between adipose and parenchymal tissue that will

also cause a random perturbation on the propagating photon wave.

Localized DOS is insensitive to random noise because a highly overdetermined system is inverted (in this implemen-tation, more than 200 measurements for two unknowns). Therefore, Eq. (3) is very robust and accurate within its assumptions. Conversely, if these assumptions are not satisfied, there may arise systematic errors that could eventually compromise the accuracy of the method. Sensi-tivity to systematic errors was reduced through the $\delta\mu_a^{Backgr}$ term. In fact, the role of $\delta\mu_a^{Backgr}$ in Eq. (3) was not to determine the average background absorption perturbation of the mixed tissue structure, because the latter was determined with DOS and not localized DOS, as will be explained in the Data Analysis section, but to account for systematic errors such as theoretical modeling uncertainties and errors in the calculation of the background optical properties. $\delta\mu_a^{Backgr}$ can also partly compensate for nonuni-form background optical property distributions that result in nonrandom wavefront perturbations. Therefore, the $\delta\mu_a^{Backgr}$ converges to a background absorption coefficient (baseline) that will contain experimental and modeling uncertainties, whereas the parameter $\delta\mu_a^{Tumor}$ fits only for correlated contrast that it is spatially consistent with the selected suspicious lesion. This performance of Eq. (3) with hetero-geneous media and its low sensitivity to its assumptions have been demonstrated [20,21].

Nevertheless, the appearance of systematic errors cannot be completely accounted for using Eq. (3). For example, spatially dependent geometrical errors, such as nonparallel compression plates, or significant deviations from a random background variation in the absorption or reduced scattering coefficients will be only partly accounted for by $\delta\mu_a^{Backgr}$ and may propagate in the calculation of $\delta\mu_a^{Tumor}$. The presence of systematic errors was examined on a per-patient basis. Spatial dependence of the breast average optical properties was investigated for each source detector pair. The typical variation of the average optical properties taken from different sides of the breast was within 10%, including experimental uncertainties. Occasionally, measurements that were converging to abnormal average optical properties, indicating deviation from a random pattern or other systematic errors, were excluded from Eq. (3).

Spectroscopy

At earlier patient examinations ($n=9$), two wavelengths were used at 780 and 830 nm. One more wavelength at 690 nm was added at more recent examinations ($n=5$). For each suspicious lesion, a system of two or three equations (depending on the number of wavelengths employed) and two unknowns (oxygenated and deoxy-genated hemoglobin concentration) was solved using direct inversion (for two equations) and quadratic fitting (for three equations). Each equation of this system is written as $\mu_a^\lambda = \varepsilon_{HBO2}^\lambda \cdot [HBO_2] + \varepsilon_{HB}^\lambda \cdot [HB] + c^\lambda$, where $\varepsilon_{HBO2}^\lambda$ and ε_{HB}^λ are the extinction coefficients for oxygenated and deoxygenated hemoglobin at wavelength λ; [HBO$_2$] [HB] are the concentrations of oxygenated and deoxygenated
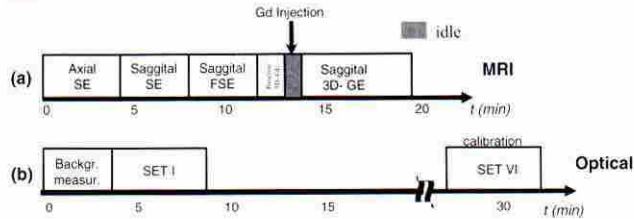
Figure 3. *The experimental simultaneous MR–optical examination protocol. Only the segments relevant to the measurement of intrinsic contrast are shown.*

hemoglobin, respectively; and c^λ is the background absorption at λ due to water and fat. The background absorptions assumed, based on water-to-lipid ratio of 2.5, were $c^{830}=0.012$ cm^{-1}, $c^{780}=0.01$ cm^{-1} and $c^{690}=0.003$ cm^{-1}. Although the third wavelength could be used to solve for c^λ, it has been shown [22] that the quantification accuracy improves if it is used in the manner employed in this work. Then the blood concentration [H] and the hemoglobin saturation Y were calculated as [H]=[HBO$_2$]+ [HB] and Y=[HBO$_2$]/[H].

Examination Protocol

The simultaneous MR and DOT study and informed consent form were approved by the institutional review board. Except for control cases, patients entering the study had a previous suspicious mammogram or palpable lesion and were scheduled for excisional biopsy or surgery. Written informed consent was obtained from all participants.

Patient placement followed standard procedures used for the MR examination. The patient assumed the prone position (Figure 1) with the breasts falling away from the chest wall and into an H-shaped coil holder. The two compression plates were positioned parallel to the sagittal plane and ensured contact of the optical fibers onto the tissue.

The simultaneous examination protocol (Figure 3) was designed so that DOT and localized DOS measurements of intrinsic (oxy- and deoxyhemoglobin) and extrinsic contrasts (intravenously administered chromophores) were performed. Here we describe only the measurements that were employed in localized DOS of oxy- and deoxyhemoglobin, as shown in Figure 2. A description of the complete examination protocol can be found elsewhere.

The MRI protocol consisted of 1) an axial T1 Spin Echo (SE) (TR/TE 500/14 FOV 24) localizer; 2) a sagittal T1-weighted SE (TR/TE 500/14 FOV 16); 3) a sagittal T2-weighted, fat-saturated fast SE (TR/TE 5000/120 FOV 16); and 4) a sagittal, three-dimensional, fat-saturated gradient echo sequence (TR/TI/TE 9.3/27/2.2, acquisition matrix 512×512 FOV 16; slice thickness 2.5–3). The last sequence (4) acquired one pre-gadolinium and three post-gadolinium sets of images to investigate the gadolinium distribution. Gadolinium was administered intravenously at 0.1 mmol/kg and demonstrated no change in the optical properties.

The localized DOS examination protocol of intrinsic contrast ran simultaneously with the MR protocol. First, a

measurement with the laser light off was performed to obtain dark current and background light noise. Then the light power was optimally adjusted so that none of the detectors was saturated. Subsequently, all sources were scanned to obtain measurements of breast intrinsic contrast (SET I). This measurement acquired the *total photon field* through the breast. At the end of the examination, a measurement on a resin phantom with absorption coefficient of $\mu_a=0.03$ cm^{-1} and $\mu'_s=10.5$ cm^{-1} at 780 nm ($\mu_a=0.028$ cm^{-1}, $\mu'_s=9.8$ cm^{-1} at 830 nm) was performed (SET VI). The phantom measurement acquired the baseline that was used to normalize the total photon field obtained through the breast [19]. The collection time for each source was 7 s.

Data Analysis

The first step was to calculate the average optical properties of the breast of each patient examined. We fitted the time domain data obtained for each source detector pair to the time-dependent solution of the diffusion equation assuming slab geometry and extrapolated boundary condition, using the Levenberg–Marquardt procedure. The specifics of the fit have been described [12]. The optical properties obtained for different source detector pairs were averaged to yield global optical properties of each breast.

The second step was to superimpose a DOT mesh on the corresponding MRI stack and segment the MRI image to the *tumor* and *background* structures. This process was performed using custom-made image analysis software developed specifically for that purpose [21]. The output of
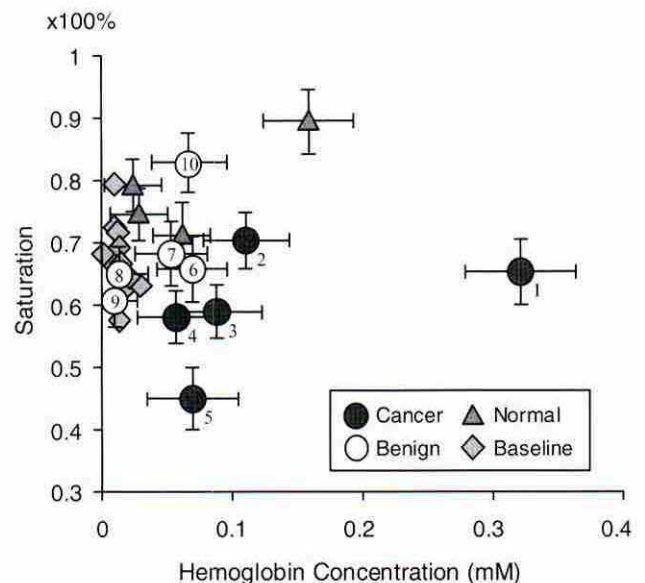

Figure 4. *Two-dimensional plot of the hemoglobin saturation and concentration measured from selected malignant and benign breast lesions using MR-guided DOS. The baseline measurements represent average values calculated from each breast examined. The normal lesions correspond to areas enhancing on MR after gadolinium administration, but were not identified as suspicious on the X-ray mammogram or diagnosed as malignant by MR.*

Table 1. MRI and Histopathological Diagnosis of the Cases Studied with Localized DOS.

Case Number	Size (cm)	MRI Diagnosis	Histopathological Diagnosis
1	0.8	Carcinoma	*In situ* and infiltrating ductal carcinoma
2	1	Diffuse carcinoma	Invasive carcinoma
3	1.2	Diffuse carcinoma	Invasive lobular carcinoma
4	1.5	Invasive carcinoma	Invasive and *in situ* ductal carcinoma
5	1.3	Carcinoma	*In situ* and infiltrating ductal carcinoma
6	1.2	Fibroadenoma	Fibroadenoma and benign breast tissue with fibrosis and focal duct hyperplasia without atypia
7	1.3	Fibroadenoma	Benign breast tissue with fibrocystic change and ductal hyperplasia
8	2	Multiple cysts	–
9	1.2	No suspicious enhancement	Fibrocystic changes with extensive stromal fibrosis
10	2.5	Ductal hyperplasia	Focal ductal hyperplasia without atypia

this process was a DOT mesh with voxels identified either as belonging to the suspicious lesion(s) or to the rest of the breast. MR segmentation was based on the first gradient echo MRI sequence acquired immediately after gadolinium administration. The typical DOT voxel selected was $3 \times 3 \times 3$ mm^3. The number of voxels varied with breast size. The suspicious lesion was manually identified for each examination on the MR stack of images using a user interface provided within the homemade image analysis program. DOT mesh voxels that coincided with the suspected lesion and were enhancing under gadolinium administration were assumed as vascular and the source of contrast for the optical examinations. Even if lesions were enhancing elsewhere in the breast, they were not included in the tumor structure. Therefore, if vascular, those lesions were contributing to the "biological" noise.

The third step was the construction of Eq. (3) and its subsequent χ^2 minimization. This minimization was the equivalent of minimizing the function $f(\overline{\delta\mu_a}) = (U - W \cdot \overline{\delta\mu_a})^2$, where $\overline{\delta\mu_a}$ is the vector of unknown perturbations in Eq. (3), U is the vector of measurements, and W is the weight matrix. The minimization process is based on the simplex algorithm provided within the MATLAB software package (Mathworks, Natick, MA). The vector of measurements is appropriately normalized using the Rytov approximation [3]. This normalization includes correction for differences in the average optical properties and thickness between the breast and the calibration phantom. The exact correction method has been reported previously [19]. We note that the weight matrix in Eq. (3) is calculated for the average optical properties of each breast examined and therefore inherently describes the average contributions of the different tissue types involved in the background structure and effectively accounts for possible lipid/adipose or other tissue compositional changes as a function of age or menstrual cycle [5] in different patients. The final output of

the fitting process was the absorption perturbations of the background and tumor structures.

The final step was the calculation of hemoglobin saturation and concentration as described in the section titled Spectroscopy.

Results

Figure 4 plots the hemoglobin saturation of the lesions investigated as a function of their hemoglobin concentration. The filled circles correspond to the five cancerous lesions encountered. The clear circles indicate benign tumors. The exact pathologies and average sizes of malignant and benign tumors are tabulated in Table 1. The triangles correspond to normal lesions that were not examined as suspicious but were retrospectively found as structures that demonstrated higher gadolinium uptake than the average background. Finally, the diamonds indicate the average saturation Y and hemoglobin concentration [H] values obtained for each breast as described in the first step of the Data Analysis section. This plot allows for a two-dimensional characterization of lesions. In general, the cancerous lesions appear of lower oxygen saturation and higher in hemoglobin concentration and they preferentially distribute in the lower right corner of the chart. Some of the normal lesions and one hyperplasia calculated also demonstrated high vascular contrast but appear significantly oxygenated. Conversely, the two fibroadenomas seen in the study yielded an increased vascular content and were also found mildly hypoxic compared to average breast hemoglobin saturation. Finally, the two cysts have a markedly low absorption that yielded a small [H] value. The average values for the cancers, the fibroadenomas, and the baseline measurements are tabulated in Table 2. One of the tumors demonstrated very high hemoglobin content but there was no evidence that this measurement was an artifact and was included in the calculations.

Figure 5 plots the hemoglobin concentration and the saturation of the cancerous lesions as a function of their size. A linear fit with and without the high [H] cancer lesion is depicted. To the extent that the limited dataset allows a conclusion, there is an apparent negative correlation between tumor size and calculated hemoglobin concentration and saturation. This observation could be explained as a decrease of vascular density due to the irregular blood vessel development, which also leads to oxygenation decrease.

The two-dimensional error bars plotted on Figure 4 indicate the standard deviation of the measurement

Table 2. Average Hemoglobin Concentration and Saturation Values of Selected Structures.

Lesion	Number of Observations	$Y \pm SD$ (%)	$[H] \pm SD$ (mM)
Cancer	5	60 ± 9	0.130 ± 0.100
Fibroadenomas	2	67 ± 2	0.060 ± 0.010
Breast tissue (baseline)	14	69 ± 6	0.018 ± 0.005

expected based on a sensitivity analysis using highly heterogeneous media [21] and assuming the signal-to-noise ratio of each experimental measurement. The sensitivity analysis also included typical systematic uncertainties, such as typical errors in the measurement of background optical properties or laser amplitude variations and jitter. Generally, the saturation calculation is sensitive to random noise because it is a ratio of two quantities but is not significantly affected by systematic errors because a small bias of both the numerator and denominator is effectively canceled out. Conversely, systematic errors propagate directly into hemoglobin concentration calculation, which is the summation of oxy- and deoxyhemoglobin. Eq. (3) is insensitive to random noise, but is susceptible to systematic errors. Therefore, total hemoglobin calculation may be less accurate than saturation calculations in this implementation if systematic errors exist in the measurement as reflected by the corresponding error bars. We also note that an unusually

large reduced scattering coefficient in the tumor structure is a systematic error and, if present, will bias more the hemoglobin concentration but not the saturation.

Discussion

The concurrent MR–DOT examination initiates a hybrid modality in which both the high-resolution structural and gadolinium enhancement pattern can be studied with MRI, but also quantified hemoglobin concentration and saturation are obtained. DOT is a complementary technique to MRI. MRI targets primarily structure, whereas DOT assesses function. MRI can also yield functional parameters such as measures of deoxyhemoglobin, but using indirect measurements of low sensitivity. The addition of localized DOS, which directly targets and quantifies oxy- and deoxyhemoglobin with high sensitivity, can significantly augment or validate measurements of hemodynamics and aid in the study of tissue functionality.

In our application, localized DOS probed the oxy- and deoxyhemoglobin content of malignant and benign breast lesions. The results seen on Figure 4 are consistent with previous studies on cancer vascularization and oxygenation [23,24]. Increased hemoglobin concentration is characteristic of increased angiogenesis, a correlate of malignant development [23]. Hypoxia has been observed with polarographic studies [25] in breast and other cancers such as head and neck and cervical cancers and is generally linked to tumoral abnormalities such as 1) compromised and anisotropic microcirculation, 2) deterioration of the diffusion geometry, and 3) tumor-associated anemia. The added features of the optical examination yield significant information for possible cancer characterization and prediction of the treatment outcome. Generally, the level of oxygenation and hemoglobin concentration of a lesion could serve as a malignant indicator to be considered with the MRI features for diagnosis and increasing the specificity of the hybrid modality. Furthermore, genetic changes that increase tumor aggressiveness and the incidence of metastases have been linked to a decrease in oxygenation [25]. Laboratory and clinical studies have suggested that hypoxia triggers the expression of the hypoxia-inducible factor 1 (HIF-1), which mediates the upregulation of angiogenic factors [26], such as the vascular endothelial growth factor (VGEF) [27], and augments the invasive and metastatic characteristics of cancers [28,29]. It has also been established that hypoxic tumors are refractory to chemotherapy or radiation therapy [30]. Therefore, the hybrid MR–optical modality can further assess important determinants for the outcome of cancer treatment because adverse clinical outcome and tumor hypoxia have been associated in clinical studies [28,29].

The purpose of this study was to demonstrate for the first time the clinical application of a novel technique and obtain an insight into the distribution of intrinsic optical contrast into tissue. Due to the small statistical sample obtained, we refrained from expanding our analysis to calculating statistical measures of sensitivity and specificity. In fact, the sensitivity of the developed hybrid modality would equal that
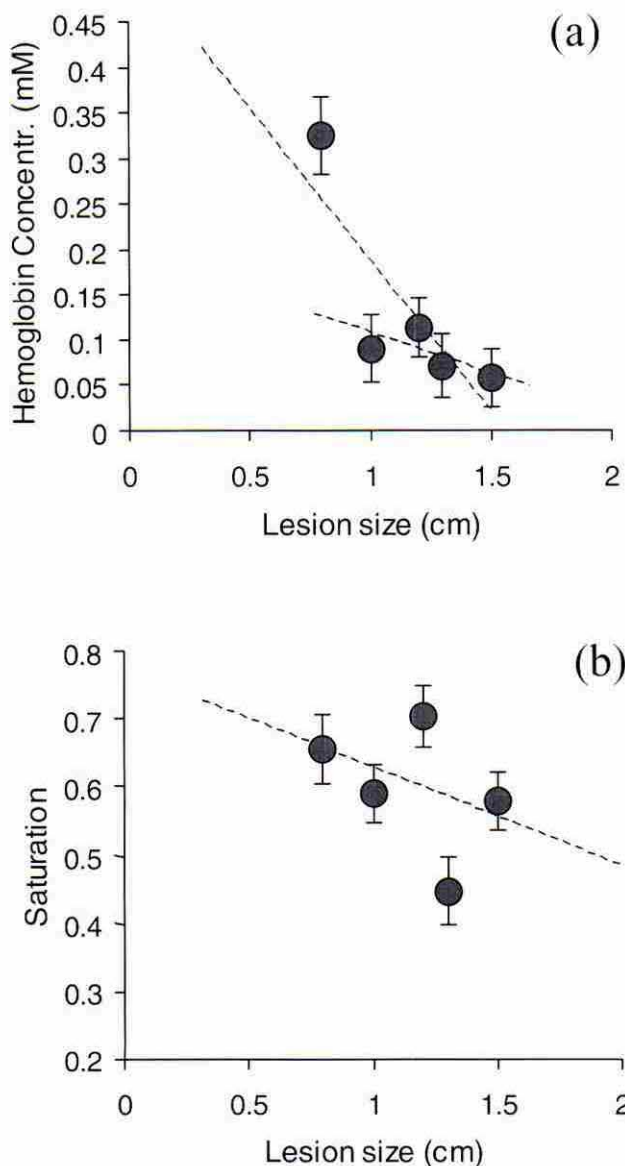

Figure 5. *Plots of (a) hemoglobin concentration and (b) saturation as a function of lesion size.*

of MRI alone because our implementation requires prior detection of a "suspicious lesion" by MRI. Whereas MRI has high sensitivity in breast cancer detection, the hybrid system could concentrate on the ability to obtain additional functional features of identified suspicious lesions that could increase the specificity of the MR examination and guide treatment strategies. These possibilities should be proved with a larger patient volume. Hopefully, this presentation could spark an interest in pursuing larger studies where the inexpensive optical technique is added to existing examination protocols for simultaneous examinations with MRI or other imaging technologies.

The hybrid examination modality can find several clinical applications besides studying breast cancer, such as assessing brain function or muscle activation. The implementation of multiple wavelengths and of higher DOT data set may be potentially used to study additional tissue absorbers of functional, pathological, or biochemical importance. Furthermore, an increased data set can allow the use of a more complex merit function so that vascular parameters of additional tissue types and tissue scattering could be independently characterized as well. Finally, the method could also find applications in the novel field of fluorescence-mediated molecular tomography [31] by similarly improving the characterization capacity of appropriate fluorescent molecular markers [32] and yield molecular characterization of deep-seated diseases in vivo.

Acknowledgements

References

[1] Chance B (1991). Optical method. Annu Rev Biophys Biophys Chem 20, 1–28.

[2] Pogue BW, Poplack SP, McBride TO, Wells WA, Osterman KS, Osterberg UL, and Paulsen KD (2001). Quantitative hemoglobin tomography with diffuse near-infrared spectroscopy: pilot results in the breast. Radiology 218, 261–66.

[3] Ntziachristos V, Yodh AG, Schnall M, and Chance B (2000). Concurrent MRI and diffuse optical tomography of breast after indocyanine green enhancement. Proc Natl Acad Sci USA 97, 2767–72.

[4] Benaron DA, Hintz SR, Villringer A, Boas D, Kleinschmidt A, Frahm J, Hirth C, Obrig H, van Houten JC, Kermit EL, Cheong WF, and Stevenson DK (2000). Noninvasive functional imaging of human brain using light. J Cereb Blood Flow Metab 20, 469–77.

[5] Tromberg B, Shah N, Lanning R, Cerussi A, Espinoza J, Pham T, Svaasand L, and Butler J (2000). Non-invasive in vivo characterization of breast tumors using photon migration spectroscopy. Neoplasia 2, 26–40.

[6] Beauvoit B, and Chance B (1998). Time-resolved spectroscopy of mitochondria, cells and tissues under normal and pathological conditions. Mol Cell Biochem 184, 445–55.

[7] Patterson MS, Chance B, and Wilson BC (1989). Time resolved reflectance and transmittance for the noninvasive measurement of tissue optical properties. Appl Opt 28, 2331–36.

[8] Hayden RE, Tavill MA, Nioka S, Kitai T, and Chance B (1996). Oxygenation and blood volume changes in flaps according to near-infrared spectrophotometry. Arch Otolaryngol, Head Neck Surg 122, 1347–51.

[9] Ferrari M, Binzoni T, and Quaresima V (1997). Oxidative metabolism in muscle. Philos Trans R Soc London, Ser B 352, 677–83.

[10] Benaron DA, Benitz WE, Ariagno RL, and Stevenson DK (1992). Noninvasive methods for estimating in vivo oxygenation. Clin Pediatr 31, 258–73.

[11] Villringer A, and Chance B (1997). Non-invasive optical spectroscopy and imaging of human brain function. Trends Neurosci 20, 435–42.

[12] Ntziachristos V, Ma XH, Yodh AG, and Chance B (1999). Multichannel photon counting instrument for spatially resolved near-infrared spectroscopy. Rev Sci Instrum 70, 193–201.

[13] Barbour R, Graber H, Chang J, Barbour S, Koo P, and Aronson R (1995). MRI-guided optical tomography: prospects and computation for a new imaging method. IEEE Comput Sci Eng 2, 63–77.

[14] Pogue BW, and Paulsen KD (1998). High-resolution near-infrared tomographic imaging simulations of the rat cranium by use of a priori magnetic resonance imaging structural information. Opt Lett 23, 1716–18.

[15] Ntziachristos V, O'Leary MA, Chance B, and Yodh AG (1996). Coregistration of images from diffusive wave with other imaging modalities to enhance optical specificity. Presented at TOPS II on Advances in Optical Imaging and Photon Migration. Orlando, FL.

[16] Ntziachristos V, Ma XH, and Chance B (1998). Time-correlated single photon counting imager for simultaneous magnetic resonance and near-infrared mammography. Rev Sci Instrum 69, 4221–33.

[17] Insko EK, Connick TJ, Schnall MD, and Orel SG (1997). Multicoil array for high resolution imaging of the breast. Magn Reson Med 37, 778–84.

[18] O'Leary MA (1996). Imaging with diffuse photon density waves. Dissertation in Physics. University of Pennsylvania, Philadelphia.

[19] Ntziachristos V, Hielscher AH, Yodh AG, and Chance B (2001). Diffuse optical tomography of highly heterogeneous media. IEEE Trans Med Imaging 20, 470–78.

[20] Ntziachristos V, Yodh AG, Schnall M, and Chance B (1998). Calculation of local optical properties in highly scattering media using a priori structural information. Presented at Photon Propagation in Tissues IV, Stockholm, Sweden.

[21] Ntziachristos V (2000). Concurrent diffuse optical tomography, spectroscopy and magnetic resonance of breast cancer. In Bioengineering. University of Pennsylvania, Philadelphia, pp. 120–27, 163–69.

[22] McBride T, Pogue BW, Osterberg U, and Paulsen KD (1999). Image reconstruction of varying objects and simulated breast cancer lesions. Presented at Optical Tomography and Spectroscopy of Tissue III. San Jose, CA.

[23] Folkman J (1994). Angiogenesis and breast cancer. J Clin Oncol 12, 441–43.

[24] Vaupel P (1997). Vascularization, blood flow, oxygenation, tissue pH, and bioenergetic status of human breast cancer. Oxygen Transp Tissue XVIII 411, 243–54.

[25] Vaupel P, and Hoeckel M (1999). Predictive power of the tumor oxygenation status. Oxygen Transp Tissue XXI 471, 533–39.

[26] Koong AC, Denko NC, Hudson KM, Schindler C, Swiersz L, Koch C, Evans S, Ibrahim H, Le QT, Terris DJ, and Giaccia AJ (2000). Candidate genes for the hypoxic tumor phenotype. Cancer Res 60, 883–87.

[27] Harmey JH, Dimitriadis E, Kay E, Redmond HP, and Bouchier-Hayes D (1998). Regulation of macrophage production of vascular endothelial growth factor (VEGF) by hypoxia and transforming growth factor beta-1. Ann Surg Oncol 5, 271–78.

[28] Brizel DM, Scully SP, Harrelson JM, Layfield LJ, Bean JM, Prosnitz LR, and Dewhirst MW (1996). Tumor oxygenation predicts for the likelihood of distant metastases in human soft tissue sarcoma. Cancer Res 56, 941–43.

[29] Hockel M, and Vaupel P (2001). Tumor hypoxia: definitions and current clinical, biologic, and molecular aspects. J Natl Cancer Inst 93, 266–76.

[30] Jain RK (1994). Barriers to drug-delivery in solid tumors. Sci Am 271, 58–65.

[31] Ntziachristos V, Tung C, Bremer C, and Weissleder R (2002). Fluorescence-mediated tomography resolves protease activity in vivo. Nat Med in press.

[32] Weissleder R (2001). A clearer vision for in vivo imaging. Nat Biotechnol 19, 316–17.